Chemical Engineering Journal 178 (2011) 306–316

Contents lists available at SciVerse ScienceDirect

Chemical Engineering Journal

journal homepage: www.elsevier.com/locate/cej

Three-dimensional binary-liquid lattice Boltzmann simulation of microchannels with rectangular cross sections

A. Kuzmin [a,*], M. Januszewski [b], D. Eskin [c], F. Mostowfi [c], J.J. Derksen [a]

[a] Chemical and Materials Engineering, University of Alberta, 7th Floor, ECERF, 9107 116 St., Edmonton, Alberta T6G 2V4, Canada
[b] Institute of Physics, University of Silesia, 40-007 Katowice, Poland
[c] Schlumberger DBR Technology Center, 9450 17 Ave. NW, Edmonton, Alberta T6N 1M9, Canada

ARTICLE INFO

Article history:
Received 27 June 2011
Received in revised form
30 September 2011
Accepted 4 October 2011

Keywords:
Taylor/Bretherton problem
Microchannel simulation
Multiphase flow
Lattice Boltzmann method
Binary liquid model
Flow in microchannels with square cross sections
Gravity driven

ABSTRACT

The classical Bretherton problem describes the propagation of gas fingers through liquid media in a narrow channel with thin liquid films between bubbles and channel walls. The bubble shape and flow patterns are complicated functions of the capillary number *Ca* and Reynolds number *Re*. Recently, we investigated the applicability and parameter selection for the two-dimensional Bretherton problem (flow between parallel plates) using the free-energy binary liquid lattice Boltzmann method (LBM) [1]. This paper is the continuation of our previous work with simulations of three-dimensional channels with rectangular (mostly square) cross sections in the range of the capillary number $0.05 \leq Ca \leq 6.0$. The flow is driven by a body force, and periodic boundary conditions are applied in the streamwise direction. The results show that the binary liquid model is able to correctly capture a number of phenomena occurring in three-dimensional capillaries, such as the existence of a vortex in front of the bubble and the way bubble radii depend on the capillary number. We conclude that lattice Boltzmann free energy binary liquid model can be used to simulate the Bretherton problem with good accuracy.

1. Introduction

The Taylor/Bretherton [2] flow deals with long gas bubbles moving through liquid in narrow channels. Depending on the channel geometry it was found [3] that the thickness of the liquid film between a bubble and channel walls is a complicated function of the capillary number *Ca*:

$$Ca = \frac{U_{\text{bubble}}\mu_{\text{liq}}}{\gamma}, \quad (1)$$

where U_{bubble} is the bubble velocity, μ_{liq} is the dynamic liquid viscosity and γ is the interfacial tension between gas and liquid.

For example, the film thickness is proportional to $Ca^{2/3}$ for small capillary numbers for circular channels [2,4]. Predicting flow patterns and associated mass transfer for Bretherton-type flows is of significant interest for chemical industry as it is widely used in chemical monolith microreactors [5]. Intensive mass transfer can be achieved because of the large interfacial area and small diffusion lengths [6]. Heat transfer is also enhanced in comparison with single phase flow [7]. While it is possible to calculate the flow analytically for small capillary numbers and nearly zero Reynolds number [2], such results cannot be extrapolated to the wide range of capillary and Reynolds numbers used in the chemical industry. Thus, the need of consistent numerical simulations arises.

Flows in two-dimensional geometries (circular tubes, parallel plates) have been studied extensively in the experimental works of Aussillous and Quere [8], and Thulasidas et al. [6], and the numerical works of Giavedoni and Saita [9], Heil [4]. All abovementioned investigations found that the Bretherton analysis is valid only for small capillary numbers $Ca \leq 0.003$ and deviates from actual measurements for larger *Ca*. This is caused by a complex interplay of gravitational, interfacial, inertial and viscous forces [3]. Historically, Bretherton [2] neglected inertia effects. Giavedoni and Saita [9] suggested that inertia effects are negligible for $Ca \leq 0.05$ and have moderate impact for $Ca > 0.05$ in the range of Reynolds number from 0 to 70 for two-dimensional flows. Later on, Heil [4] studied the flow between plates up to $Re = 300$. This author noted that while the influence of inertia on the established film thickness is insignificant (7% deviation from the film thickness measured at $Re = 0$), the change in Reynolds number significantly influences the pressure distribution and the flow field near the front bubble cap. Thulasidas et al.[6] showed that the mass transfer is strongly affected by flow direction for small capillary numbers in case of upward and downward flows. Thus, to fully describe the propagation of the

* Corresponding author. Tel.: +1 7807293695.
E-mail addresses: kuzmin@ualberta.ca, shurik.kuzmin@gmail.com (A. Kuzmin), michalj@gmail.com (M. Januszewski), deskin@slb.com (D. Eskin), fmostowfi@slb.com (F. Mostowfi), jos@ualberta.ca (J.J. Derksen).

1385-8947/$ – see front matter © 2011 Elsevier B.V. All rights reserved.
doi:10.1016/j.cej.2011.10.010

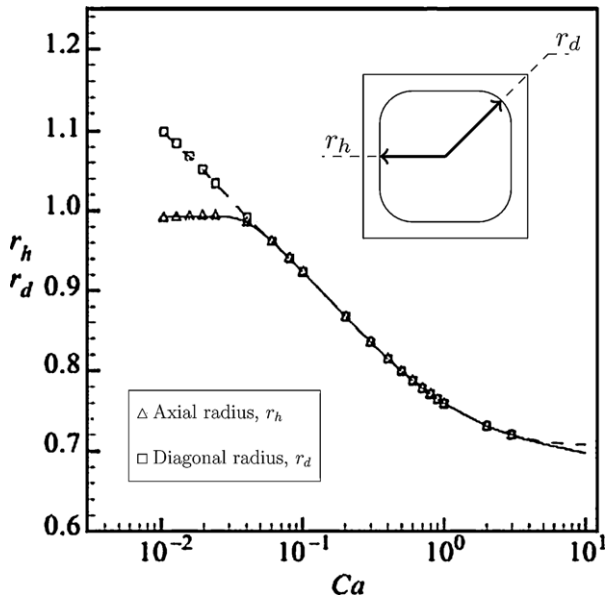

Fig. 1. Hazel and Heil [11] results for the variation of the bubble radii for a range of capillary numbers for a square channel. One can see the asymmetry between diagonal and axial diameters for the capillary numbers $Ca \leq \widehat{Ca} = 0.04$. Courtesy of Hazel and Heil [11]. r_h and r_d are scaled on the half side length $H_{\text{eff}}/2$.

semi-infinite finger in liquid media one needs to take into account the viscous, gravitational, surface, and inertia forces [3].

In comparison with the two-dimensional Bretherton flows (circular tubes, flow between plates), there is a vast number of experimental results available for three-dimensional flows in microchannels with square, triangular and rectangular cross sections. For instance, Thulasidas et al. [6] performed a number of experiments for a bubble-train flow in capillaries of square cross sections for horizontal, upward and downward flows. Han and Shikazono [10] obtained experimental results for the film thickness dependence on the capillary number for ethanol/air and water/air mixtures and for square, circular and triangular shaped microchannels. They also presented an experimental correlation for bubble radii based on the capillary number Ca and the Weber number $We = Re\,Ca$, where the Reynolds number is defined as:

$$Re = \frac{U_{\text{bubble}} H_{\text{eff}}}{\nu_{\text{liq}}}, \tag{2}$$

where H_{eff} is the channel height and ν_{liq} is the kinematic liquid viscosity.

The experimental works [10,6] supported by numerical simulations [11,12] showed interesting phenomena in three-dimensional geometries. It was found [11,13] that for rectangular capillaries there is a transition from an asymmetric to an axisymmetric shape for a certain capillary number. The non-axisymmetric shape describes the wall normal radius (in Fig. 3 the wall normal radius is measured along x or y axes) being different from the diagonal radius and the bubble having a non-circular shape in the channel cross section. In this case, the bubble shape mimics the shape of a rectangle and looks like a rectangle with rounded corners. Further we adapt the convention "axial" for the radius measured along the x or y axes, see Fig. 3 [11]. The dependence of the diagonal and axial radii or a square channel on the capillary number is shown in Fig. 1. The capillary number for square channels at which transition between non-axisymmetric case to axisymmetric happens is reported in a number of works ($\widehat{Ca} = 0.04$ [6], $\widehat{Ca} = 0.1$ [14,12], $\widehat{Ca} = 0.033$ [11]). If the capillary number is larger than the critical capillary number, i.e. $Ca > \widehat{Ca}$, then the bubble becomes axisymmetric with the radius of the bubble dependent on the capillary number. An example for the bubble radii dependence on the capillary number is presented in Fig. 1.

There are also a number of numerical works on three-dimensional flows. For instance, Wong et al. [13,15] studied three-dimensional bubbles in polygonal capillaries and calculated bubble shapes for different slug and channel cross sections. Hazel and Heil [11] performed three-dimensional simulations for circular-, square- and rectangular-shaped capillaries. They indicated a transition of flow regime in a liquid slug. Vortexes observed at lower capillary numbers disappear as the capillary number goes beyond a certain threshold, Fig. 6. For a square channel the critical capillary number is $Ca = 0.691$. Hazel and Heil [11] also found an empirical correlation which makes it possible to collapse results of radii dependency on the capillary number for rectangular channels with different aspect ratios on a single curve. It was also found that for microchannels with a certain aspect ratio $\alpha = a/b \geq 2.04$, the interface does not become circular for any capillary number. Liu and Wang [12] performed numerical simulations using the Volume of Fluid (VOF) technique for capillaries with non-circular (square, triangular) cross sections. They also investigated the relative slug to bubble velocity for a range of capillary numbers.

As was mentioned by Gupta et al. [3], the most common techniques to simulate the Bretherton phenomena are the VOF method [12], the level-set method [7] and the finite element methods [16,11]. It was also indicated [3] that the new techniques, which are still in the development stage, are the lattice Boltzmann method and phase field methods [17,18]. The finite element method solves the Bretherton flow as a free-surface problem with a sharp interface but without gas. The lattice Boltzmann method is a continuous interface method, and therefore provides more flexibility in simulations involving coalescence and/or droplet breakup, and thus arises as a promising alternative for simulation of gas finger propagation.

In our previous work [1], we already analyzed the Bretherton flow between parallel plates. It was shown that the free-energy binary liquid model, which is a phase field method, simulates the Bretherton/Taylor phenomenon with reasonable accuracy. The goal of this work is to examine if similar conclusions can be drawn for three-dimensional flows in microchannels with square cross sections, simulated using the free-energy binary liquid lattice Boltzmann method.

The lattice Boltzmann method has emerged as a successful method to simulate a wide variety of phenomena including hydrodynamics [19], thermal flows [20], microflows [21], ferrofluids [22], and multiphase flows [23,24]. It is a particle method which allows one to simulate physical phenomena on the microscopic level. For instance, the introduction of a force or a potential on the microscopic level makes it possible to restore multiphase macroscopic equations [23,24]. Nowadays the method is finding its way to more practical applications, for example magnetically driven droplet break-up and vaporization [25], mixing in cross-channel flow [26], etc.

The binary liquid free-energy LB model due to Swift et al. [23] that we used simulates two liquids with the assumption of uniform overall density. The classical Bretherton problem is stated for gas and liquid, which are of significantly different density and viscosity. In general, a system is correctly simulated if all its non-dimensional parameters match those of the corresponding real physical system. However, one needs to consider the leading non-dimensional numbers which are responsible for physical phenomena. Even though the binary-liquid model cannot match the gas–liquid density ratio, we consider it as a non-leading parameter. This is justified by the numerical results of Giavedoni and Saita [9] and Heil [4] which show negligible Reynolds number effects on the film thickness for a relatively wide range of Reynolds numbers, $Re < 70$. The parameters in our simulations were carefully chosen to avoid inertia effects, see Section 2. The maximum attained Reynolds number is $Re < 10$.

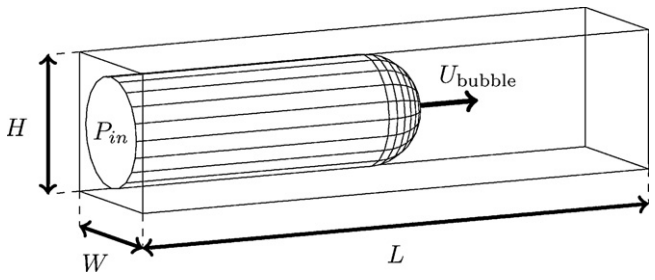

Fig. 2. The classical benchmark layout describes a semi-infinite gas bubble propagation through the liquid media. The inlet pressure is specified P_{in}, the outlet is the free outflow. The bubble propagates with constant velocity U_{bubble}.

A second reason is the fact that density ratio is involved in the description of the bubble shape change. There is a corresponding number defining the shape change called the Bond number and defined as $Bo = CaRe/Fr^2$. For real microchannel systems the Bond number is less than 0.1 and we can neglect the bubble shape change due to the density difference. Therefore, the major governing factor for microchannel flows is not the density ratio, but the viscosity ratio, which explains why the uniform density binary liquid model is suitable for this kind of simulations.

Note that other multiphase lattice Boltzmann models can be used which can account for different densities, such as the pseudopotential-based approach [27] or the color model [23]. In the case of the pseudopotential-based approach, one needs to use the binary-liquid formulation to avoid possible condensation/evaporation [28] and to perform Laplace law simulations to calibrate the surface tension as it is not given explicitly. For the case of the color model, one needs to use more complicated schemes to reconstruct the surface. However, one can use the same procedure of setting up simulations for all above-mentioned models.

One should acknowledge the works of Ledesma-Aguilar et al. [29] on menisci in thin films for fingering phenomena. Yang et al. [30] performed lattice Boltzmann simulations of two-dimensional channel flows for relatively large capillary numbers, and found discrepancies with the classical Bretherton theory, which is limited to the low capillary number regime [9]. They used the Shan-Chen model, which is sometimes said to contain a thermodynamically inconsistent interface [31].

The paper is organized as follows. First, we explain the simulation benchmark construction mainly based on our previous work [1]. Then, the binary liquid lattice Boltzmann model is outlined. The simulation results for the three-dimensional case are presented in the results section. That covers the film thickness dependency on the capillary number, the bubble to slug relative velocity and vortex profiles for square microchannels. We also briefly cover flow simulations for rectangular channels. The paper is concluded with a summary of the main findings.

2. Numerical benchmark approach

The main discussion here is based on the two-dimensional benchmark approach [1]. It was indicated that the benchmark layout should have certain dimensions to conduct simulations. The classical Bretherton benchmark layout is represented in Fig. 2. It describes the gas finger propagation through the liquid medium. The film thickness in this case is measured at the inlet. In the lattice Boltzmann framework, such a formulation has certain challenges [1]. Some of them are attributed to the dynamic coupling of the inlet and outlet conditions [9]. Instead, we proposed the numerical benchmark indicated in Fig. 3. The dimensions of the channel are chosen as $H_{\text{eff}} \times H_{\text{eff}} \times 15H_{\text{eff}}$. The initial bubble length

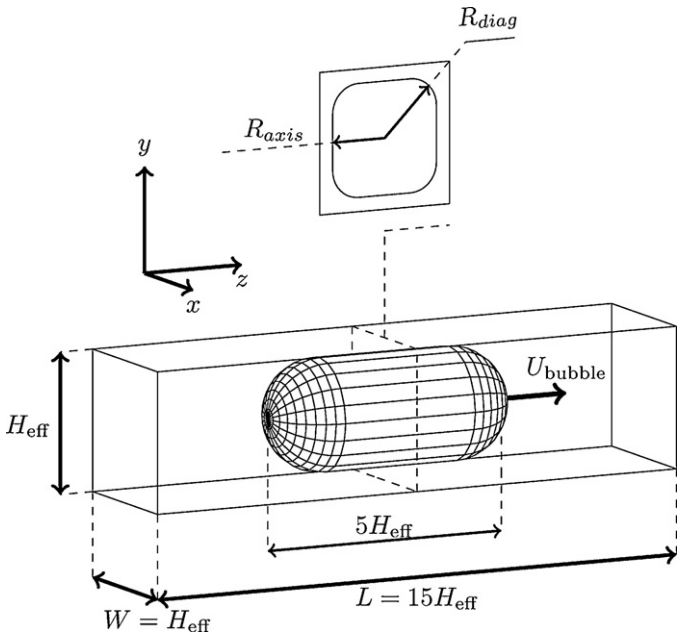

Fig. 3. The lattice Boltzmann benchmark layout as used in present calculations. The dimensions of the domain are chosen as $H_{\text{eff}} \times H_{\text{eff}} \times 15H_{\text{eff}}$. The length of the bubble was chosen as $5H_{\text{eff}}$ for the film thickness to stabilize. Periodic boundary conditions are applied in the streamwise direction. The flow is driven by a body force.

is taken as $5H_{\text{eff}}$. Giavedoni and Saita [9] showed that the film in the two-dimensional geometry stabilizes at distances of 2.6–4.0 diameters from the front tip depending on the Reynolds number. Hazel and Heil [11] measured the bubble radii at the distance of $5.5H_{\text{eff}}$ and indicated it to be sufficient for $Ca \leq 10$. In this work, the following relation holds for all conducted simulations: $0.05 \leq Ca \leq 6$. Thus, the film thickness is chosen to be measured in the middle of the bubble, which is located at least at a distance of 2.5–3 channel heights from the bubble tip.

For simplicity, periodic boundary conditions are applied. Therefore a bubble train is simulated instead of a single bubble. The mutual influence of neighbouring bubbles is minimized by using a long channel ($15H_{\text{eff}}$). Periodic boundary conditions imply as well that the fluid is driven by a body force in the framework of the LBM and not with a pressure difference. Therefore, we cannot address simulations with upward and downward flows [6] which would require a simultaneous imposition of pressure boundary conditions and the body force.

It was indicated [1] that the film thickness for two-dimensional simulations should be at least twice as large as the interface thickness. The interface thickness occupies 3–5 nodes due to the continuous interface formulation of the binary liquid model. Therefore, the film should be resolved as at least 6–10 nodes.

Hazel and Heil [11] and Fig. 1 specify that the diagonal bubble radius is different from the axial bubble radius for $Ca \leq \widehat{Ca} \approx 0.03$. The radii are approximately the same for larger values of Ca with a value $R_{diag} = R_{axis} = 0.49H_{\text{eff}}$. Therefore, taking the minimal requirement for the film thickness to be resolved, i.e. 6 lattice nodes, one would obtain a grid size of $600 \times 600 \times 9000$ to properly resolve the binary liquid flow. This size implies that relatively large computational resources are required to perform the simulations. However, as it will be shown later the film thickness in the simulations is larger than the example number ($0.49H_{\text{eff}}$ for $Ca \approx 0.03$). Therefore, actual grids are smaller (indicated in Section 4) than the computationally too demanding grid of $600 \times 600 \times 9000$.

One can argue that a non-uniform grid could be used. However, the film thickness is a function of the curvatures of the front bubble tip [2] and the grid would need to be refined just at the interface between gas and liquid. This is complicated to achieve for dynamic systems where a bubble moves in the streamwise direction. To reduce the computational overhead, we decided to take a simpler approach and exploit the inherent symmetry of the problem by simulating only a quarter of the channel (see Appendix B for details).

It should be noted that the binary liquid model we used has a uniform density. This issue was partially addressed in the introduction: to describe the Bretherton problem one needs to take into account gravitational, viscous, inertial, and surface tension forces. Among all the works, there is no full agreement between results even in the limit of Reynolds number zero. Moreover, as was indicated by Kreutzer et al. [16] and by Thulasidas et al. [6] the pressure distribution, streamlines and bubble shape are strongly affected by the length of the liquid slug and the length of the bubble. In the current simulations we minimize the effects of bubbles train and inertia. Inertia effect are minimized as the largest Reynolds number is not bigger than 10. The mutual effects of bubbles motion on each other is minimized by choosing lengths of a bubble and a channel large enough in comparison with the channel height. However, more thorough studies are needed in order to understand precisely the above-mentioned effects.

3. Binary liquid lattice Boltzmann model

The lattice Boltzmann equation (LBE) operates on a rectangular grid representing the physical domain. It utilizes probability distribution functions (also known as particle populations) containing information about macroscopic variables, such as fluid density and momentum. LBE consists of two parts: a local collision step, and a propagation step which transports information from one node to another in certain directions specified by a discrete velocity set. The LBE is typically implemented as follows [32]:

$$\begin{aligned} f_i^*(\boldsymbol{x},t) &= \omega f_i^{eq}(\boldsymbol{x},t) - (1-\omega) f_i(\boldsymbol{x},t) + F_i, && \text{collision step} \\ f_i(\boldsymbol{x}+\boldsymbol{c_i}, t+1) &= f_i^*(\boldsymbol{x},t), && \text{propagation step} \\ g_i^*(\boldsymbol{x},t) &= \omega_\phi g_i^{eq}(\boldsymbol{x},t) - (1-\omega_\phi) g_i(\boldsymbol{x},t), && \text{collision step} \\ g_i(\boldsymbol{x}+\boldsymbol{c_i}, t+1) &= g_i^*(\boldsymbol{x},t), && \text{propagation step,} \end{aligned} \tag{3}$$

where $\{f,g\}_i$ are the probability distribution functions in the direction $\boldsymbol{c_i}$, ω is the relaxation parameter, ω_ϕ is the phase relaxation parameter, and F_i is the external force population responsible for force inclusion to the Navier–Stokes equation.

The binary fluid LB model is based on a free-energy functional [23,33], and operates with two sets of populations: one (f_i) to track the pressure and the velocity fields, and another (g_i) to represent the phase field ϕ indicating gas or liquid. The equilibrium populations [34] are defined as:

$$\begin{aligned} f_i^{eq} &= w_i(3p_0 - k\phi\Delta\phi + \frac{u_\alpha c_{i\alpha}}{c_s^2} + \frac{Q_{i\alpha\beta}u_\alpha u_\beta}{2c_s^4}) + k w_i^{\alpha\beta}\partial_\alpha\phi\partial_\beta\phi, \quad 1 \le i \le Q-1 \\ f_0^{eq} &= \rho - \sum_{i\neq 0} f_i^{eq} \\ g_i^{eq} &= w_i\left(\Gamma\mu + \frac{\phi c_{i\alpha}u_{i\alpha}}{c_s^2} + \phi\frac{Q_{i\alpha\beta}u_\alpha u_\beta}{2c_s^4}\right), \quad 1 \le i \le Q-1 \\ g_0^{eq} &= \phi - \sum_{i\neq 0} g_i^{eq}, \end{aligned} \tag{4}$$

where Γ is the mobility parameter; the chemical potential $\mu = -A\phi + A\phi^3 - k\Delta\phi$; k is a parameter related to the surface tension; A is a parameter of the free-energy model; Q is the number of directions (19 for the $D3Q19$ model); the tensor $Q_{i\alpha\beta} = c_{i\alpha}c_{i\beta} - c_s^2\delta_{\alpha\beta}$ with the sound speed parameter $c_s^2 = 1/3$. The bulk pressure is expressed as $p_0 = c_s^2\rho + A(-0.5\phi^2 + 0.75\phi^4)$. The discrete velocity set is defined as:

$$\begin{aligned} c_{ix} &= \{0,1,-1,0,0,0,0,1,-1,1,-1,0,0,0,0,1,-1,1,-1\} \\ c_{iy} &= \{0,0,0,1,-1,0,0,1,1,-1,-1,1,-1,1,-1,0,0,0,0\} \\ c_{iz} &= \{0,0,0,0,0,1,-1,0,0,0,0,1,1,-1,-1,1,1,-1,-1\}. \end{aligned} \tag{5}$$

The weights are $w_0 = 0, w_{1-6} = 1/6$ and $w_{7-18} = 1/12$. The weights related to the inclusion of the surface tension are:

$$\begin{aligned} &w_{1-2}^{xx} = w_{3-4}^{yy} = w_{5-6}^{zz} = \frac{5}{12} \\ &w_{3-6}^{xx} = w_{1-2,5-6}^{yy} = w_{1-4}^{zz} = -\frac{1}{3} \\ &w_{7-10,15-18}^{xx} = w_{7-14}^{yy} = w_{11-18}^{zz} = -\frac{1}{24} \\ &w_{11-15,}^{xx} = w_{15-18}^{yy} = w_{7-10}^{zz} = \frac{1}{12} \\ &w_{7,10}^{xy} = -w_{8,9}^{xy} = w_{11,14}^{yz} = -w_{12,13}^{yz} = w_{15,18}^{zx} = -w_{16,17}^{zx} = \frac{1}{4}. \end{aligned} \tag{6}$$

The set of equations (4) restores the macroscopic fluid equations as:

$$\begin{aligned} &\partial_t\rho + \partial_\alpha\rho u_\alpha = 0 \\ &\rho\left(\partial_t + u_\beta\partial_\beta\right)u_\alpha = F_\alpha - \partial_\beta P_{\alpha\beta} + \nu\partial_\beta\left(\rho\partial_\alpha u_\beta + \rho\partial_\beta u_\alpha\right) \\ &\partial_t\phi + \partial_\alpha\phi u_\alpha = M\partial_{\beta\beta}^2\mu, \end{aligned} \tag{7}$$

where $\nu = c_s^2(\tau - 1/2)$ is the kinematic viscosity, $M = \Gamma(\tau_\phi - 1/2)$ is the mobility parameter, and $\tau = 1/\omega$ and $\tau_\phi = 1/\omega_\phi$ are the relaxation parameters of density and phase fields. The first equation of system (3) simulates the continuity equation and the Navier–Stokes equation. The lattice Boltzmann equation for the second set g_i simulates the phase propagation with the supplied velocity from the Navier–Stokes equation.

The system allows the separation of the liquid phase with $\phi = 1$ and a so-called gas phase with $\phi = -1$. The relaxation time is taken to be linearly dependent on the relaxation times τ_{gas} and τ_{liq}: $\tau = \tau_{gas} + ((\phi+1)/2)(\tau_{liq} - \tau_{gas})$. This makes it possible to smoothly change viscosity from the gas viscosity $\nu_{gas} = (1/3)(\tau_{gas} - (1/2))$ to the liquid viscosity $\nu_{liq} = (1/3)(\tau_{liq} - (1/2))$ in a region where a phase gradient exists. The surface tension in the framework of the binary liquid model is $\sqrt{8kA/9}$. The walls were simulated using the bounce-back rule [19]. The walls were taken with neutral wettability as the studied effects are wettability-independent [1]. Moreover, there is no two/three phase contact line where wettability plays a crucial role.

4. Results

This section describes numerical simulations. We refer to Appendix A for initialization and scaling procedures. The simulations were conducted on the following fluid domain grids $100\times100\times1500$, $160\times160\times1500$, $160\times160\times2400$ and $200\times200\times3000$. Body forces were varied as $dP/dz = 10^{-6}$–10^{-4} lattice units. The binary-liquid model parameters were kept in the stable region $k = A = 0.04$ for most simulations and $k = A = 0.004$ for simulations with $Ca = 6.70$. Note that the choice of $k = A$ guarantees that the film thickness is 5 grid spacings, which is a good choice for stability reasons. The relaxation rates were taken as $\tau_{liq} = 2.5$ and $\tau_{gas} = 0.7$ giving a gas-over-liquid viscosity ratio of 10. The relaxation parameter for the phase field was $\tau_\phi = 1.0$.

First, we examine when the steady-state is reached. Then, the critical capillary number is identified where the transition

Table 1
Results for the steady-state case. One can see that 200,000 steps are enough to shape the bubble and approach the steady state. The small noise in the capillary number is connected to the identification of the interface and spurious currents in the system. The spurious currents influence the bubble velocity identification which is taken at the front bubble tip. The binary liquid model is the continuous interface model. Thus one needs to interpolate phase function data to obtain the location of the bubble interface $\phi = 0$ and its velocity. Thus, there is a larger deviation for capillary numbers. All other parameters are relaxed to the steady-state.

N_{iter}	Ca	R_{axis}	R_{diag}
140,000	0.1879	0.8657	0.8708
150,000	0.1879	0.8652	0.8704
160,000	0.1878	0.8650	0.8702
170,000	0.1880	0.8648	0.8701
180,000	0.1882	0.8647	0.8700
190,000	0.1885	0.8646	0.8699
20,0000	0.1893	0.8645	0.8698
210,000	0.1963	0.8645	0.8697
220,000	0.1925	0.8644	0.8697
230,000	0.1936	0.8644	0.8697
240,000	0.1961	0.8645	0.8697
250,000	0.1932	0.8645	0.8698

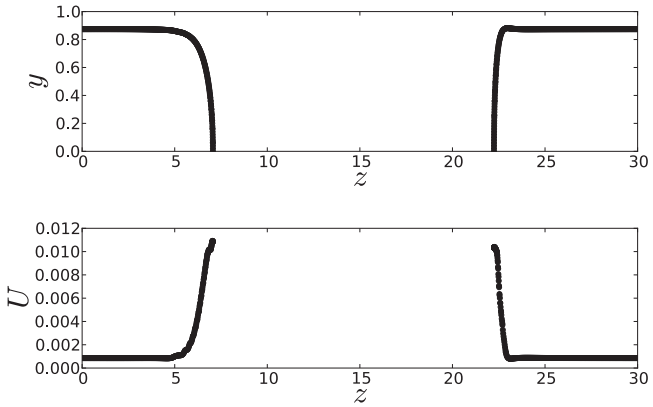

Fig. 4. The bubble shape and the corresponding streamwise velocities taken on the bubble interface after 240,000 iterations. Directions y and z are scaled to the half of the channel $H_{\text{eff}}/2$. One can see that the bubble front and rear caps are propagating with nearly the same velocity, that is the actual bubble velocity. For more details on velocity patterns see Section 4.3.

from the non-symmetrical to axisymmetrical bubble shape occurs. The dependency of the radii on the capillary number is presented for the range of moderate capillary numbers $0.05 \leq Ca \leq 6.0$. Results are concluded with studies of the velocity pattern.

4.1. Steady-state approach

We performed different simulations to understand the number of time steps required for the system to settle down to a steady state. The grid was $52 \times 52 \times 750$ which represents a quarter of the channel with the initial film thickness of 6.5 lattice units together with the body force $dP/dx = 1.6 \times 10^{-6}$. The simulation was performed for 250,000 iterations with the step of 10,000 iterations. The results for time iterations 140,000–250,000 are summarized in Table 1. While the capillary number variation is around 5%, the radii variation is 0.1%. Note, that the interface velocity is defined as the bubble tip velocity in the microchannel center. Multiphase lattice Boltzmann models is known to have spurious currents near the interface [35,36]. Therefore, the bubble interface velocity is influenced by spurious currents and capillary numbers show larger variation than radii.

To further examine the steady-state, the velocity in the streamwise direction is plotted. The values of the velocity are taken on the contour where $\phi = 0$. This corresponds to the bubble interface. That allows to check whether the bubble is propagating as a whole rigid body or it's shrinking or elongating. This is one of the characteristics of the steady-state. One can see in Fig. 4 the contour plot and the corresponding streamwise velocity component. The cross section is a plane $x = 0$, where x points towards the reader, z is the streamwise direction. As fluxes inside the bubble have clockwise and counterclockwise directions, see Section 4.3, one needs to thoroughly examine only the points corresponding to the front and the rear bubble caps. If they are equal, then it is exactly the velocity with which the bubble propagates in the microchannel as a rigid body. For a physical analogy, one can imagine the rotating ball propagating in the streamwise direction. The front and rear ball points have the same streamwise velocity.

4.2. Radii transition

Due to computational power restrictions we can only access the region of $Ca \geq 0.05$. In this region the proper resolution of the film thickness is achievable. To identify the critical capillary number $\widehat{Ca}$ a number of simulations were conducted, see Table 2. In comparison with the results of the Hazel and Heil [11] ($\widehat{Ca} = 0.04$) our results are closer to the VOF continuous interface method simulation by Liu and Wang [12] ($\widehat{Ca} = 0.1$). Due to linear approximation we consider a bubble to have a circular cross section if R_{axis} and R_{diag} differ by less than 1%. The transition for current simulations happens for $Ca \approx 0.09$ calculated as linear interpolation between data presented in Table 2. One can see two examples of non-axisymmetric and axisymmetric bubble shapes for $Ca = 0.053$ and $Ca = 1.13$, see Fig. 5.

4.3. Velocity pattern

The liquid velocity pattern is known to change its behavior depending on the capillary number. For relatively low capillary numbers $Ca < 0.6$, in a reference frame moving with the bubble a vortex is observed [11]. For larger capillary numbers it is indicated that there is no vortex in front of the bubble. The transition capillary number specified by Hazel and Heil [11] for a square channel as $Ca = 0.691$. However, the distribution of vorticity strongly depends on the Reynolds number [4], as well as on the pressure distribution. In the case of the bubble train it is indicated by Kreutzer et al. [16] that the pressure is significantly influenced by bubble frequency and slug distance. The present simulations are conducted for bubble trains and certain differences in terms of changing streamline patterns are expected. We examined velocity patterns to identify the moment of the streamlines pattern change. We chose two representative capillary numbers as $Ca = 0.47$ and $Ca = 0.63$. One can

Table 2
Simulation results in terms of R_{axis} and R_{diag} for the transition region between non-axisymmetric and axisymmetric cases. The transition occurs at $\widehat{Ca} = 0.09$, which is a linear interpolation between data with radii not equal and equal to each other. The grid for simulations was chosen as $50 \times 50 \times 1500$ for a quarter of a channel. That means that the corresponding interpolation error of determining radii is a half of the reverse grid number, $1/2N_x = 0.01$. Thus, if radii values are within 1% we consider them equal to each other. We also included a corresponding Reynolds number to show that inertia effects can be neglected.

Ca	R_{axis}	R_{diag}	Re
0.053	0.95	1.01	0.907
0.078	0.93	0.95	1.062
0.102	0.91	0.91	1.392
0.132	0.89	0.89	1.80

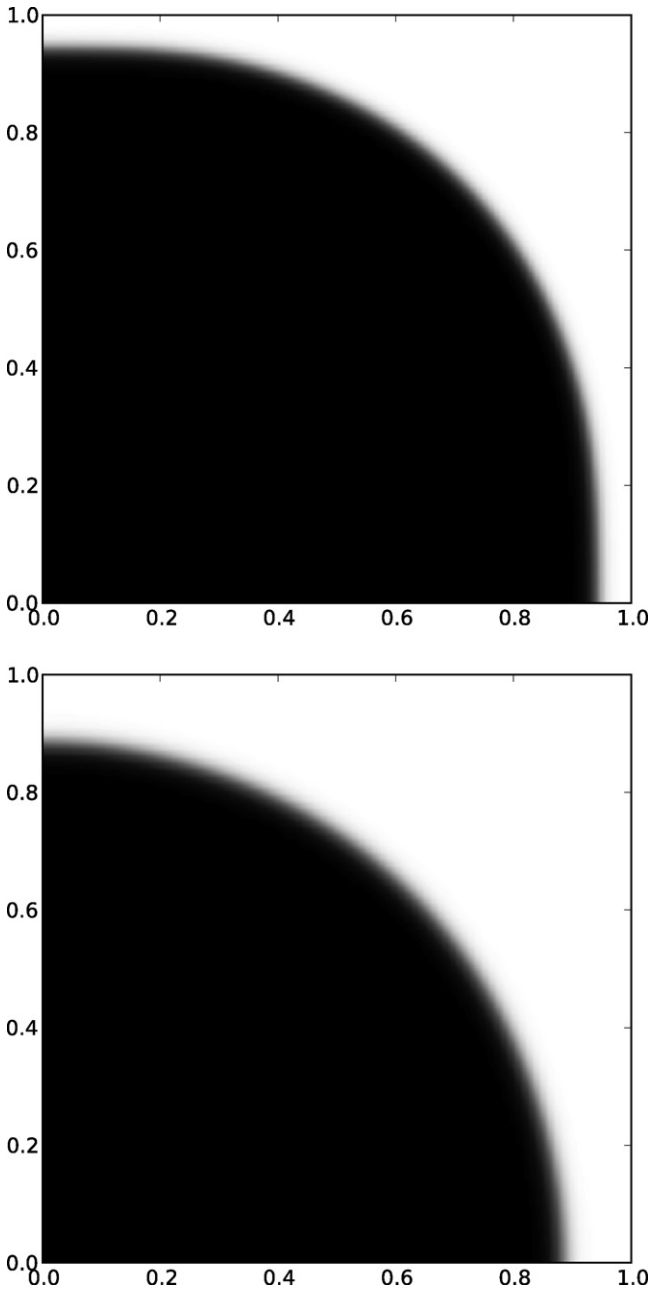

Fig. 5. Cross sections of the phase field in the middle of the bubble for $Ca = 0.053$ (top) and $Ca = 1.13$ (bottom). Cross sections are rescaled on the half channel height. Other parameters are indicated in Table 2. One can see that the left picture is non-axisymmetric in contrast with the right one, i.e. $R_{diag} \neq R_{axis}$. The transition happens at $\widehat{Ca} = 0.09$.

see in Fig. 6 a clear transition between associated patterns. Among all different simulation runs with different grids and initial conditions, the transition occurs at $Ca = 0.6$–0.7, see Fig. 6. The transition is identified between regimes where there exists and does not exist a vortex in the slug. Either all streamwise slug velocities have the same sign (no vortex), or have different signs (vortex). It is indicated by Kreutzer et al. [4,37] that the bubble train flow depends on the slugs and bubbles lengths. Thus, we expect the difference of bubble train simulations and simulations of a semi-infinite air finger propagation [11]. The transition also depends on the identification of the bubble velocity which is influenced by spurious currents and interpolation errors.

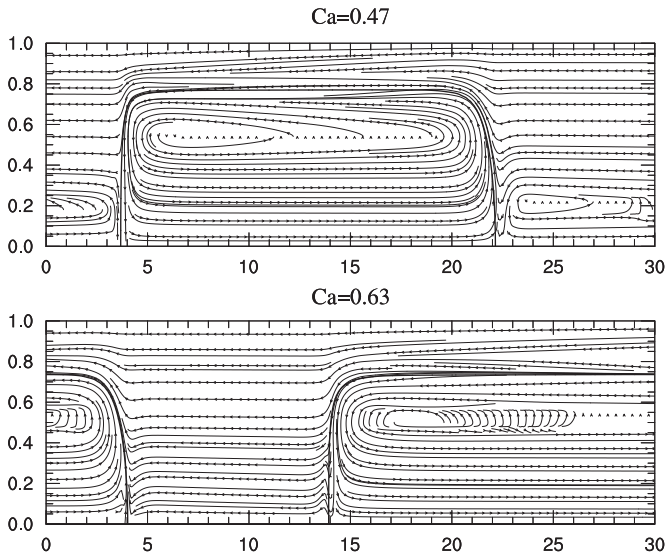

Fig. 6. Velocity vector maps for $Ca = 0.47$ and $Ca = 0.63$. One can see that there are no vortexes created in front of the bubble for $Ca = 0.63$. For presented simulations the transition happens between $Ca = 0.47$ and $Ca = 0.63$, which is a different value from $Ca = 0.69$ [11]. However, we performed a number of different types of simulations (different force, width initialization). The critical transition capillary number $\widehat{Ca}$ is not well fixed and varies from $\widehat{Ca} = 0.6$–0.7.

4.4. Variation over bubble length

The work of Liu and Wang [12] shows the variation of the bubble radii along the bubble. The bubble shape in terms of axial and diagonal radii is reconstructed for a number of capillary numbers, Fig. 7. One can see that for smaller capillary numbers the diagonal radius exhibits a small jump near the rear bubble cap. That agrees with results of Liu and Wang [12]. However, our simulations show smoother behavior of the jump.

Another interesting phenomenon regarding the bubble shape was indicated by Hazel and Heil [11]. In their simulations the non-axisymmetric shape was observed even for larger capillary numbers $Ca > 4$ near the bubble front cap which after certain distance relaxes to have radii equal to each other. The bubble shape was calculated for the large capillary number $Ca = 6.43$, see Fig. 8.

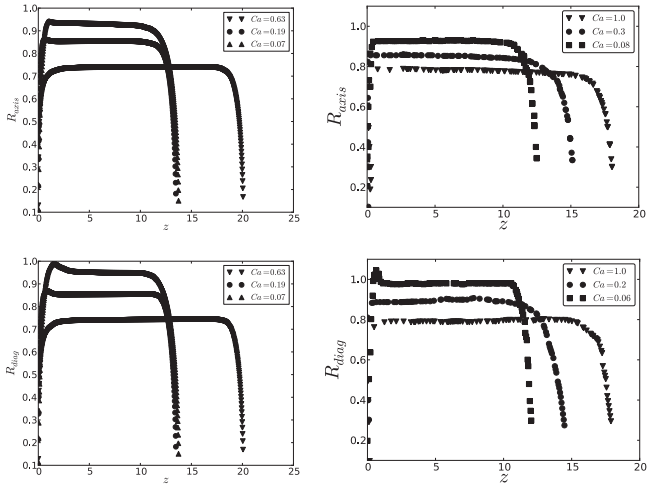

Fig. 7. Simulations radii variations (left) along the bubble for different capillary numbers in the plane $x = 0$. One can see that the diagonal radius shows the jump near the bubble rear cap. This agrees with the VOF simulations of Liu and Wang [12] (right). Coordinate z increases in the streamwise direction. The discretization of Liu and Wang [12] data was performed with "Engauge Digitizer".

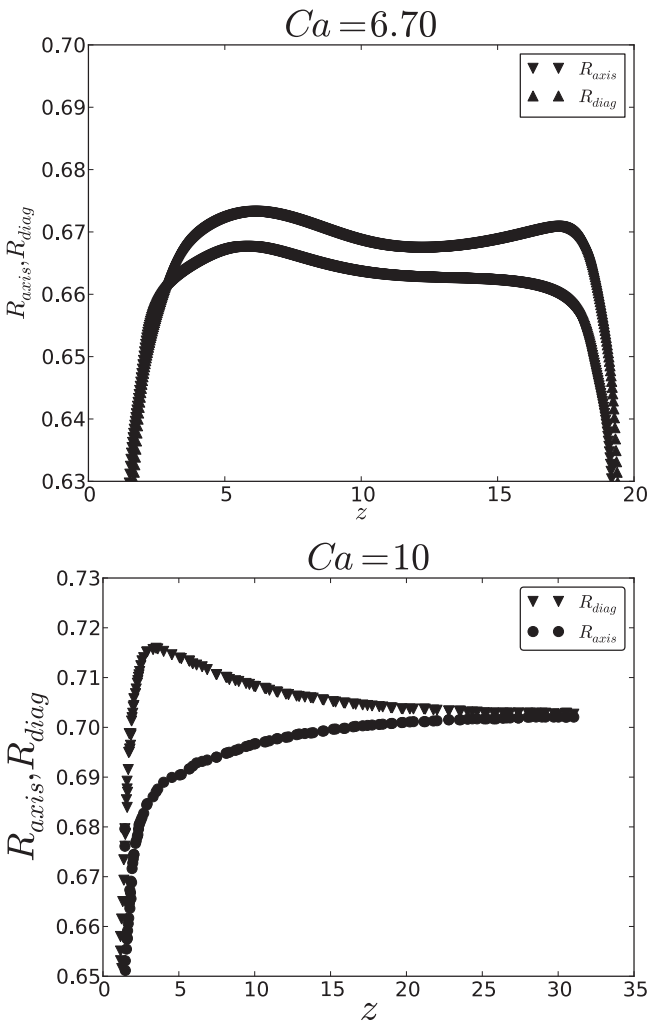

Fig. 8. The bubble shape for the capillary number $Ca = 6.43$ is presented (top). z increases in the streamwise direction. One can see that near the front tip (large z) the diagonal radius exhibits a jump which is relaxed to the axis radius (small z). Even though this resembles the shape of the curves obtained by Hazel and Heil [11] (bottom, opposite streamwise direction), there is a difference between radii of the current simulation (top) of around 1%, which can be attributed to the linear interpolation used in the calculation of the interface.

However, even the diagonal radius shows the jump near the front tip of the bubble and it resembles the shape given by Hazel and Heil [11], but the difference is around 1% and can be explained by error in the linear interpolation used for the interface calculation. Therefore, we do not observe the symmetry breakage for $Ca > 4$.

4.5. Capillary number

The purpose of this section is to study dependence of the radii on the capillary number. The film thicknesses were extracted from the middle of the bubble. The data presented in Fig. 9 is simulated with different techniques including different initialization, and different grids: $52 \times 52 \times 1500$, $82 \times 82 \times 1500$ and $82 \times 82 \times 2400$. All our results are consistent and show grid and initialization independence. Therefore one can conclude that for the capillary number $Ca \geq 0.05$ grid independence is achieved. The results are compared with the results of Hazel and Heil [11] and of Liu and Wang [12]. The data were extracted from the corresponding references with the help of the program "Engauge Digitizer". We observe that lattice Boltzmann simulations exhibit the transition between non-axisymmetric and axisymmetric shape of the bubble.

The present simulations show that the corresponding critical capillary number is close to $\widehat{Ca} = 0.1$ that agrees with the work of Liu and Wang [12] and is different from the results of Hazel and Heil [11], $\widehat{Ca} = 0.04$. However, in the range of the moderate capillary numbers our results are closer to the results of Hazel and Heil [11] and exhibit less noisy trend in radii values and a more accurate transition between non-axisymmetric and axisymmetric cases than results of Liu and Wang [12].

4.6. Relative velocity

One of the differences between the flow in tubes and square capillaries is that the flow has different streamline patterns. In square microchannels, the main mass flow occurs through corners [11,12]. This affects the mass flow significantly. One of the characteristics of the mass flow is the normalized dependence of the relative velocity on the capillary number. The bubble always moves faster than the surrounding liquid. The following quantity is defined as relative velocity [6]:

$$W = \frac{U_{\text{bubble}} - U_{ls}}{U_{\text{bubble}}}, \tag{8}$$

where U_{bubble} is the bubble interface velocity, and U_{ls} is the liquid superficial velocity. As far as the steady state is achieved one can take the liquid superficial velocity exactly at the cross section in the middle between bubbles. The liquid superficial velocity is defined as:

$$U_{ls} = \frac{\int_A U_{\text{liq}}\, dA}{A}. \tag{9}$$

The relative velocity was calculated and compared with the results of Hazel and Heil [12], see Fig. 10. One can see an agreement between the simulations indicating that one of the mass transport characteristics can be captured accurately.

The relative velocity is an important quantity of mass flow characterization [16,38]. However, there are other important characteristics that significantly influence the mass transfer, i.e. the frequency of the bubbles [16] and inertia effects [4]. Future work is planned to study this phenomenon and calculate the mass transfer coefficient by solving the advection-diffusion equation.

4.7. Rectangular channel simulations

While the main focus of this paper is on the square microchannel simulations, we performed a number of simulations for rectangular channels with varying aspect ratio $\alpha = W/H_{\text{eff}} = a_x/a_y$, where a_x and a_y are sides of the rectangular in x and y directions. Hazel and Heil [11] performed a number of simulations for the propagation of semi-infinite air finger in the microchannel. They indicated that the radii in x and y directions are increasing with the aspect ratio α increases. The same trend can be seen for the current simulation results, see Fig. 11. One can see that diagonal and axial radii are not the same as they were in square channels for the capillary number range investigated here. The same is indicated by Hazel and Heil [11] who mentioned that for radii to coincide one needs to have really long bubbles, at least 100 shorter semi-axis bubble length for the aspect ratio $\alpha = 1.5$. This is not possible to achieve with the current bubble train simulations.

They as well indicated that the simulations results with different aspect ratio can be put on one curve by calculating non-dimensional

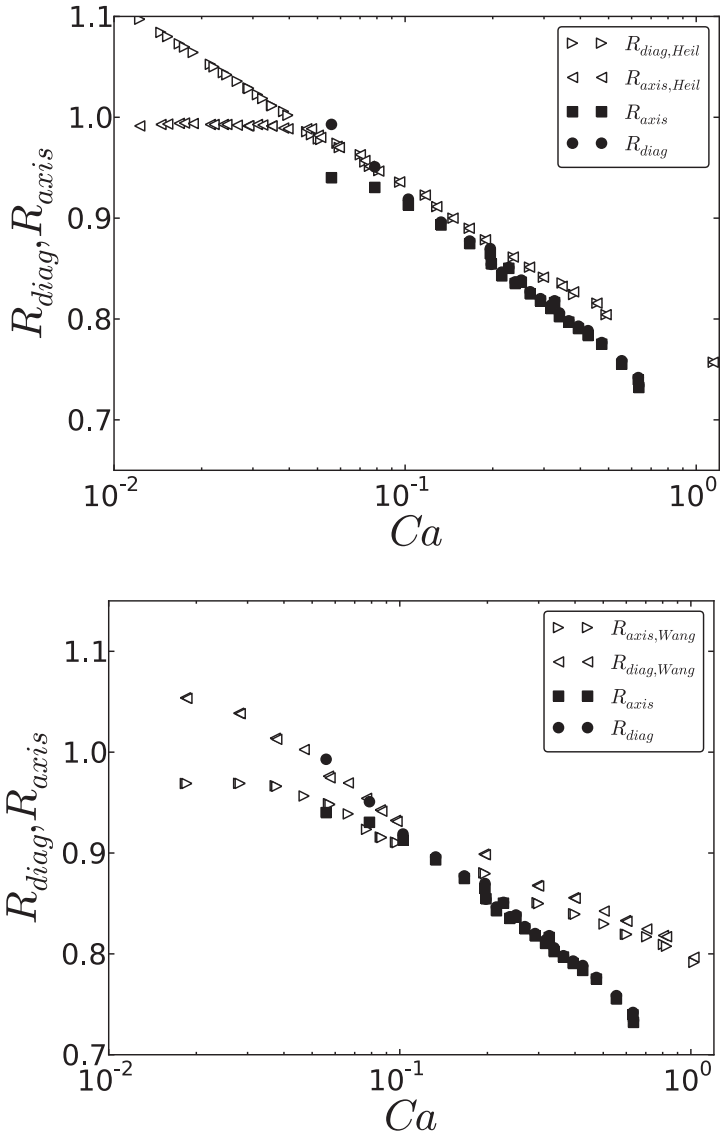

Fig. 9. The comparison for the axial and the diagonal radii versus capillary numbers between present simulations and the results of Hazel and Heil [11] (top), of Liu and Wang [12] (bottom). One can see that the code mimics behavior of the earlier published results.

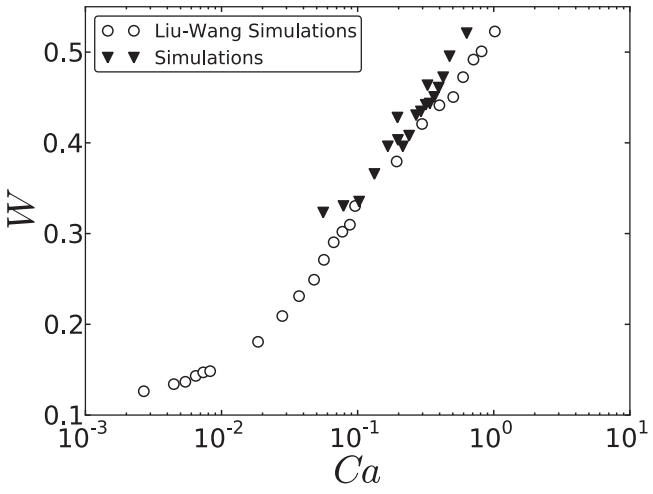

Fig. 10. Relative velocity comparison between current simulations and simulations of Liu and Wang [12]. One can see a qualitative agreement.

radius s_∞ that scales different aspect ratio microchannels. It is based on the calculation of r_∞ (the radius that the air finger will have at an infinite distance from the bubble tip):

$$\frac{r_\infty}{H_{\text{eff}}/2} = \frac{\sqrt{Q/\pi}}{H_{\text{eff}}/2}$$
$$s_\infty = \frac{r_\infty}{H_{\text{eff}}/2}\alpha^{-1/2}, \tag{10}$$

where Q is the area occupied by air in the cross section. Hazel and Heil [11] indicated a simple physical interpretation of this phenomena: providing that air is injected with the same velocity to the channels with different aspect ratio but the same area, the resulting occupied area by the bubble should not depend on the aspect ratio. That is quite interesting phenomena indicating that if bubbles are infinite long then they would have the same radius and will be circular. The current results, see Fig. 12 show that this hypothesis can be extended for bubble train flows with different radii $R_h \neq R_v$.

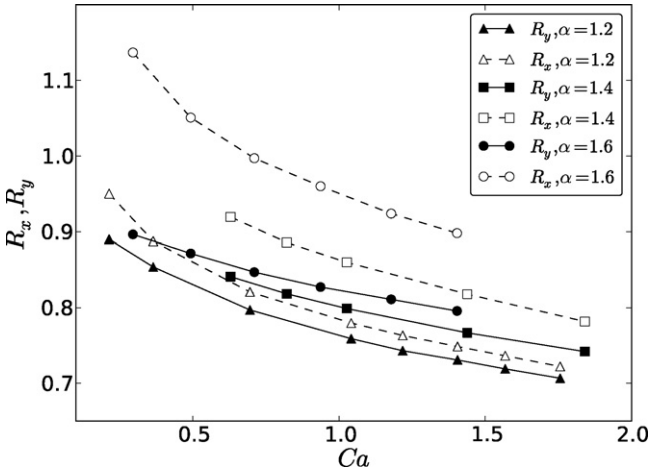

Fig. 11. Radii in x (R_x) and y (R_y) directions for rectangular microchannels with different aspect ratios. Radii are rescaled on the length of channel in y direction. One can see that with the increase of α the radii increase as well. However, $R_x \neq R_y$. It was indicated by Hazel and Heil [11] one needs semi-infinite bubble to achieve $R_x = R_y$.

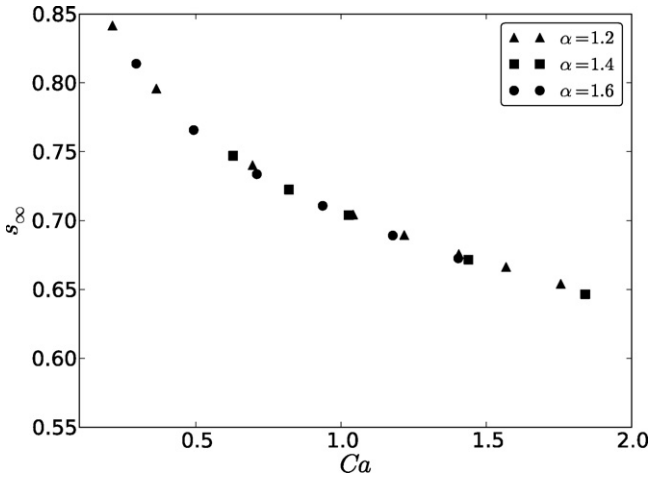

Fig. 12. The non-dimensional radius s_∞ for different aspect ratio rectangular microchannels. One can see that all the curves coincide independently of the aspect ratio.

5. Conclusion

This work presents results of binary-liquid simulations for three-dimensional channels with square cross sections with the lattice Boltzmann method. By resolving properly the film thickness as twice the interface thickness [1] the results were shown to be consistent with those available in the literature. Note that the literature results show some variations. This work falls within the range of data presented in the literature. For instance, the transition from the non-axisymmetric to the axisymmetric case is shown to be at $\widehat{Ca} = 0.09$ which is close to results of Liu and Wang [12]. However, in the moderate range of parameters simulation results are close to the results of Hazel and Heil [11] and exhibit more accurate transition between non-axisymmetric and symmetric cases than results of Liu and Wang [12]. Overall, the film thickness dependency on the capillary number, the transition from the non-axisymmetric to symmetric case, and the velocity patterns were investigated. While the goal of this work is a feasibility study, more numerical studies are needed to understand the influence of the slug length, inertia effects, pressure distributions [16,38] on the design of microchannels. Our results show that the lattice Boltzmann binary liquid model can be used for simulation of gas bubbles in microchannels.

Appendix A. Scaling procedure

The scaling procedure has been extensively described in our previous work [1]. Here, we present only an outline of how the simulations are initialized:

Capillary number: One first needs to set the capillary number and the Reynolds number for simulations.

Film thickness: After the capillary number is prescribed, one needs to approximate the axial bubble radius R_{axial}, the corresponding film thickness is $\delta = 1 - R_{axial}$. One can use correlations of Han and Shikazono [10] or of Kreutzer et al. [16]. It can also be done by taking correlations from numerical simulations by Heil [4] and Giavedoni and Saita [9].

Grid choice: After specifying the film thickness, one needs to choose the number of nodes to resolve the film thickness. For binary liquid parameters used in simulations, $k = A = 0.04$ and $k = A = 0.004$ the interface is spread over approximately 5 lattice units. To obtain grid independent results one needs to choose the film thickness to be 2–2.5 times larger than the interface thickness [1]. Given the number of nodes to resolve the film thickness and given the lattice Boltzmann benchmark, see Section 2, one can obtain the grid dimensions.

Velocity: The Reynolds and capillary numbers are supplied from the physical world:

$$Ca = \frac{U_{\text{bubble}}\mu_{\text{liq}}}{\gamma}$$
$$Re = \frac{U_{\text{bubble}}H_{\text{eff}}}{\mu_{\text{liq}}}. \quad \text{(A.1)}$$

In Eq. (A.1) the interface tension coefficient is prescribed by parameters of the binary liquid model k and A, the effective channel height H_{eff} is obtained from the film thickness resolution, μ_{liq} is defined through the relaxation rate τ_{liq}. The relaxation rate τ_{liq} is prescribed from the gas–liquid viscosity ratio $\mu_{\text{liq}}/\mu_{\text{gas}}$, where μ_{gas} is defined through the gas relaxation rate τ_{gas}. The parameter $\tau_{\text{gas}} \geq 0.5$, therefore constraining the linked parameter τ_{liq}. Moreover, the stability of the lattice Boltzmann scheme is known to deteriorate with the relaxation parameter $\tau_{\text{liq,gas}} \approx 0.5$ [39]. On the other hand the accuracy of the lattice Boltzmann liquid model deteriorates as $(\tau_{\text{liq,gas}} - (1/2))^2$ [40]. Thus, there is a compromise of the choice of parameters τ_{liq} and τ_{gas}. The gas–liquid viscosity ratio in the current simulations was chosen as $\mu_{\text{liq}}/\mu_{\text{gas}} = \nu_{\text{liq}}/\nu_{\text{gas}} = 10$ and the relaxation parameters were chosen to be in the safe region, i.e. $\tau_{\text{liq}} = 2.5$ and $\tau_{\text{gas}} = 0.7$.

Given the considerations of the relaxation parameters, one can obtain the desired bubble velocity U_{bubble} from the equation for the Reynolds number (A.1). Substituting the bubble velocity U_{bubble} to the definition of the capillary number, Eq. (A.1), one can obtain the interface tension which is connected with the binary liquid

parameters k and A. The stability of the lattice Boltzmann scheme implies the simultaneous change of τ_ϕ with the change of parameters k and A [41]. Therefore, if Reynolds number is less than 50–100 one can neglect the inertia effects and obtain the bubble velocity straight from the capillary number limiting the complex interplay of the parameters for the LBM simulations to be stable:

$$U_{\text{bubble}} = Ca\frac{\gamma}{\mu_{\text{liq}}} = Ca\frac{\sqrt{8kA/9}}{1/3(\tau_{\text{liq}} - (1/2))}, \tag{A.2}$$

where usually $k = A = 0.004, 0.04$.

Body force: It is desired to obtain the prescribed velocity U_{bubble} in simulations. Since the flow in the simulations is driven by a body force, a connection between this force and the bubble velocity U_{bubble} has to be established. We assume that the flow is close to the planar Poiseuille flow with U_{bubble} being the maximum in the Poiseuille profile for the square shaped microchannels:

$$\frac{dP}{dz} = \frac{\mu_{\text{liq}} U_{\text{bubble}}}{\sum_{i\le 0, j\le 0}(16/\pi^6)((-1)^i(-1)^j)/((2i+1)(2j+1)[(2i+1)^2/W_{\text{eff}}^2 + (2j+1)^2/H_{\text{eff}}^2])}. \tag{A.3}$$

Though the Poiseuille profile assumption works reasonably well [1], instead of calculating sums (A.3) we suggest to simply start simulations with the body force $dP/dz = 10^{-6} - 10^{-5}$ for grids of size $50 \times 50 \times 1500$ and the capillary number $Ca \approx 0.1$–6.0.

After imposing the body force the simulations can be run. A typical simulation runs approximately 100,000–300,000 time steps to reach steady-state, see Section 4.1. To design the simulations one needs to keep proportionality between parameters through the equations above. For example if one knows the capillary number Ca_1 and the corresponding body force dP_1/dz for simulations conducted on the grid with the characteristic number of nodes N_{y1}, the body force for another simulation can be calculated as:

$$\frac{dP_1/dx}{dP_2/dx} = \frac{Ca_1}{Ca_2}\frac{N_{y2}^2}{N_{y1}^2} \tag{A.4}$$

Appendix B. Symmetric boundary conditions

To reduce the computational load in terms of memory and CPU power by a factor of 4, we performed the simulation of only a quarter of the channel using symmetric boundary conditions. The scalar macroscopic variables at the boundary nodes have the same values as those of the adjacent fluid nodes. The same applies for tangential velocities U_τ, while velocities perpendicular to the mirror boundary U_n have opposite signs to that of the velocity of the fluid node. This can be summarized as:

$$\rho_B = \rho_F, \quad \phi_B = \phi_F, \quad U_{B\tau} = U_{F\tau}, \quad U_{Bn} = U_{Fn}, \tag{B.1}$$

where the subscripts B and F stand for the boundary and the nearest fluid node, respectively.

For the lattice Boltzmann model the incoming populations on the boundary node need to be specified. For generality we assume that the symmetry plane is $\alpha = 0$, where α is the direction x or y. Then, for lattice Boltzmann populations the symmetric boundary conditions can be expressed through the following steps:

I: Identify complementary directions. For the direction i' to be complementary to the ith direction, the following relations must hold:

$$\begin{aligned} c_{i\alpha} &= -c_{i'\alpha}, \quad \text{where } \alpha = \text{ is the symmetry plane} \\ c_{i\beta} &= -c_{i'\beta}, \quad \text{where } \beta \neq \alpha. \end{aligned} \tag{B.2}$$

Note that the complementary directions for the directions parallel to the symmetry plane coincide with the original direction.

II: Take the distributions from the nearest fluid node and apply them to the boundary node utilizing the complementary directions:

$$f_{i,B} = f_{i',F}. \tag{B.3}$$

It can easily be seen that the procedure described above conserves the scalar fields and the tangential velocity, while reversing the normal flux. The plane of symmetry is located half-way between fluid and boundary nodes.

References

[1] A. Kuzmin, M. Januszewski, D. Eskin, F. Mostowfi, J.J. Derksen, Simulations of gravity-driven flow of binary liquids in microchannels, Chem. Eng. J. 171 (2) (2011) 646–654.
[2] F.P. Bretherton, The motion of long bubbles in tubes, J. Fluid Mech. 10 (2) (1960) 166–188.
[3] R. Gupta, D.F. Fletcher, B.S. Haynes, Taylor flow in microchannels: a review of experimental and computational work, J. Comput. Multiphase Flows 2 (2010) 1–32.
[4] M. Heil, Finite Reynolds number effects in the Bretherton problem, Phys. Fluids 13 (9) (2001) 2517–2521.
[5] M.T. Kreutzer, M.G. van der Eijnded, F. Kapteijn, J.A. Moulijn, J.J. Heiszwolf, The pressure drop experiment to determine slug lengths in multiphase monoliths, Catal. Today 105 (2005) 667–672.
[6] T.C. Thulasidas, M.A. Abraham, R.L. Cerro, Bubble-train flow in capillaries of circular and square cross section, Chem. Eng. Sci. 50 (2) (1995) 183–199.
[7] K. Fukagata, N. Kasagi, P. Ua-arayaporn, T. Himeno, Numerical simulation of gas–liquid two-phase flow and convective heat transfer in a micro tube, Int. J. Heat Fluid Flow 28 (2007) 72–82.
[8] P. Aussillous, D. Quere, Quick deposition of a fluid on the wall of a tube, Phys. Fluids 12 (10) (2000) 2367–2371.
[9] M.D. Giavedoni, F.A. Saita, The axisymmetric and plane cases of a gas phase steadily displacing a Newtonian liquid – a simultaneous solution of the governing equations, Phys. Fluids 9 (8) (1997) 2420–2428.
[10] Y. Han, N. Shikazono, Measurement of liquid film thickness in micro square channel, Int. J. Multiphase Flows 35 (2009) 896–903.
[11] A.L. Hazel, M. Heil, The steady propagation of a semi-infinite bubble into a tube of elliptical or rectangular cross-section, J. Fluid Mech. 470 (2002) 91–114.
[12] D. Liu, S. Wang, Hydrodynamics of Taylor flow in noncircular capillaries, Chem. Eng. Process. 47 (2008) 2098–2106.
[13] H. Wong, C.J. Radke, S. Morris, The motion of long bubble in polygonal capillaries. Part 1. Thin films, J. Fluid Mech. 292 (1995) 71–94.
[14] W.B. Kolb, R.L. Cerro, Film flow in the space between a circular bubble and a square tube, J. Colloids Interface Sci. 159 (1993) 302–311.
[15] H. Wong, C.J. Radke, S. Morris, The motion of long bubbles in polygonal capillaries. Part 2. Drag, fluid pressure and fluid flow, J. Fluid Mech. 292 (1995) 95–110.
[16] M.T. Kreutzer, F. Kapteijn, J.A. Moulijn, C.R. Klejn, J.J. Heiszwolf, Inertial and interfacial effects on pressure drop of Taylor flow in capillaries, AIChE J. 51 (9) (2005) 2428–2440.
[17] D.M. Anderson, G.B. McFadden, A.A. Wheeler, Diffuse-interface methods in fluid mechanics, Annu. Rev. Fluid Mech. 30 (1998) 139–165.
[18] E. Gurtin, D. Polignone, J. Vinals, Two-phase binary fluids and immiscible fluids described by an order parameter, Math. Models Methods Appl. Sci. 6 (6) (1996) 815–831.
[19] D. Yu, R. Mei, L.-S. Luo, W. Shyy, Viscous flow computations with the method of lattice Boltzmann equation, Prog. Aerosp. Sci. 39 (2003) 329–367.
[20] S. Ansumali, I.V. Karlin, H.C. Öttinger, Minimal entropic kinetic models for hydrodynamics, Europhys. Lett. 63 (6) (2003) 798–804.
[21] S. Ansumali, I.V. Karlin, C.E. Frouzakis, K.B. Boulouchos, Entropic lattice Boltzmann method for microflows, Physica A 359 (2006) 289–305.
[22] G. Falcucci, G. Chiatti, S. Succi, A.A. Mohamad, A. Kuzmin, Rupture of a ferrofluid droplet in external magnetic fields using a single-component lattice Boltzmann model for nonideal fluids, Phys. Rev. E 79 (056706) (2009) 1–5.

[23] M.R. Swift, W.R. Osborn, J.M. Yeomans, Lattice Boltzmann simulation of non-ideal fluids, Phys. Rev. Lett. 75 (5) (1995) 831–834.
[24] X. Shan, H. Chen, Simulation of nonideal gases and gas–liquid phase transitions by the lattice Boltzmann equation, Phys. Rev. E 49 (4) (1994) 2941–2948.
[25] G. Falcucci, S. Succi, S. Ubertini, Magnetically driven droplet break-up and vaporization: a lattice Boltzmann study, J. Stat. Mech. 2010 (5) (2010) 1–10.
[26] J.J. Derksen, Simulations of lateral mixing in cross-channel flow, Comput. Fluids 39 (2010) 1058–1069.
[27] M. Sbragaglia, R. Benzi, L. Biferali, S. Succi, K. Sugiyama, F. Toschi, Generalized lattice Boltzmann method with multirange potential, Phys. Rev. E 75 (026702) (2007) 1–13.
[28] C.M. Pooley, H. Kusumaatmaja, J.M. Yeomans, Modeling capillary filling dynamics using lattice Boltzmann simulations, Eur. Phys. J. Spec. Top. 171 (2009) 63–71.
[29] R. Ledesma-Aguilar, I. Pagonabarraga, A. Hernàndez-Machado, Three-dimensional aspects of fluid flows in channels. II. Effects of meniscus and thin film regimes on viscous fingers, Phys. Fluids 19 (102113) (2007) 1–8.
[30] Z.L. Yang, B. Palm, B.R. Sehgal, Numerical simulation of bubbly two-phase flow in a narrow channel, Int. J. Heat Mass Transfer 45 (2002) 631–639.
[31] B.R. Sehgal, R.R. Nourgaliev, T.N. Dinh, Numerical simulation of droplet deformation and break-up by lattice-Boltzmann method, Prog. Nucl. Energy 34 (4) (1999) 471–488.
[32] I. Ginzburg, F. Verhaeghe, D. d'Humières, Two-relaxation-time Lattice Boltzmann scheme: about parameterization, velocity, pressure and mixed boundary conditions, Commun. Comput. Phys. 3 (2) (2008) 427–478.
[33] L. Landau, E. Lifshitz, Fluid Mechanics, Oxford, Pergamon, 1987.
[34] C.M. Pooley, H. Kusumaatmaja, J.M. Yeomans, Contact line dynamics in binary lattice Boltzmann simulations, Phys. Rev. E 78 (056709) (2008) 1–9.
[35] C.M. Pooley, K. Furtado, Eliminating spurious velocities in the free-energy lattice Boltzmann method, Phys. Rev. E 77 (046702) (2008) 1–9.
[36] X. Shan, Analysis and reduction of the spurious current in a class of multiphase lattice Boltzmann models, Phys. Rev. E 73 (047701) (2006) 1–4.
[37] M.T. Kreutzer, F. Kapteijn, J.A. Moulijn, J.J. Heiszwolf, Multiphase monolith reactors: chemical reaction engineering of segmented flow in microchannels, Chem. Eng. Sci. 60 (2005) 5895–5916.
[38] J. Yue, L. Luo, Y. Gonthier, G. Chen, Q. Yuan, An experimental study of air–water Taylor flow and mass transfer inside square microchannels, Chem. Eng. Sci. 64 (2009) 3697–3708.
[39] A. Kuzmin, I. Ginzburg, A.A. Mohamad, A role of the kinetic parameter on the stability of the two-relaxation-times advection-diffusion lattice Boltzmann schemes, Comput. Math. Appl. 61 (12) (2011) 3417–3442.
[40] I. Ginzburg, F. Verhaeghe, D. d'Humières, Study of simple hydrodynamic solutions with the two-relaxation-times lattice Boltzmann scheme, Commun. Comput. Phys. 3 (3) (2008) 519–581.
[41] V.M. Kendon, M.E. Cates, I. Pagonabarraga, J.-C. Desplat, P. Bladon, Inertial effects in three-dimensional spinoidal decomposition of a symmetric binary fluid mixture: a lattice Boltzmann study, J. Fluid Mech. 440 (2001) 147–203.